AIAA JOURNAL
Vol. 36, No. 9, September 1998

Global/Local Postbuckling Failure Analysis of Composite Stringer/Skin Panels

H. Alesi,* V. M. Nguyen,† and N. Mileshkin‡
Royal Melbourne Institute of Technology, Melbourne, Victoria 3001, Australia
and
R. Jones‡
Monash University, Clayton, Victoria 3168, Australia

A finite element methodology for postbuckling failure analysis of composite stringer/skin panels is presented. The methodology employs a global two-dimensional plate finite element model for representing overall panel deformation and a local three-dimensional solid finite element model for representing stress within a critical panel region. Global and local models are connected with a two-dimensional/three-dimensional coupling methodology that is based on multipoint constraints. Analyses are carried out for two different panel designs utilizing both linear and nonlinear material models. Computational results for failure load, failure location, and failure mode compare favorably with results from earlier experimental test programs. The findings suggest that failure initiation in postbuckled composite stringer/skin panels can be effectively modeled with the developed finite element methodology.

Nomenclature

$D_0, n, f_1, f_2, m, Z_0, Z_1, \Omega_s, C_P$ = material model parameters
E = Young's modulus
G = shear modulus
h = solid node distance from plate midplane
K_2 = overstress
N = local value of shape function
P = point force
$\boldsymbol{R}^{**}$ = rotation matrix
S_{ij} = deviatoric stress
u, v, w = translational degrees of freedom
X, Y, Z, S, R, T = material allowables
x, y, z = orthogonal coordinate axes
Z = drag stress
ε_e^I = effective inelastic strain
ε_{ij} = strain
$\dot{\varepsilon}_{ij}^I$ = inelastic strain rate
η, ξ = intrinsic coordinates
ν = Poisson's ratio
σ_{ij} = applied stress
$\varphi_x, \varphi_y, \varphi_z$ = rotational degrees of freedom
Ω_{ij} = back stress
0 = global coordinate system index
$\cdot$ = time derivative
$*$ = modified postyield slope

Introduction

ONE approach for reducing aircraft structural weight is to employ graphite/epoxy composites with high strength-to-weight and/or high stiffness-to-weight ratios for the primary structure. However, to date it is not possible to utilize the full strength of these materials because they are generally not allowed to be employed in postbuckling structures such as stringer/skin panels. Buckling of these structures is prevented by limiting the design strain. This restriction is necessary in part because reliable postbuckling failure analysis tools do not exist.

Previous work on stiffened carbon/epoxy panels established that failure initiation often commences within the skin/stiffener region. The current assumption is that overall panel failure starts with localized ply delaminations in this region that are induced by three-dimensional stresses.

During the past decade computational models have been developed for analyzing three-dimensional stresses at critical interfaces of composite stringer/skin panels. Finite element (FE) models employing two-dimensional interface elements and quasi-three-dimensional models fall into this category. These models, although computationally efficient, often involved considerable simplification of the structural geometry, which in turn complicated the engineering interpretation of results. This problem may be overcome with global two-dimensional/local three-dimensional modeling techniques as suggested by Card and Starnes.[1] Herewith the global part of a structure is modeled with two-dimensional plate FEs, and only a critical local domain is modeled with three-dimensional solid FEs (Fig. 1). The authors developed a postbuckling failure analysis methodology that is based on this approach.[2] The methodology is applied in the current work for the analysis of failure in two different composite stringer/skin panels.

Coupling Methodology

Global two-dimensional and local three-dimensional models for the panels analyzed are connected with a new coupling methodology. The new methodology is based on a multipoint constraint approach. Kinematic constraints are thereby imposed by guiding plate boundary nodes onto a dependent solid element node. Constraints are defined according to solid node location relative to the plate element boundary.

The fundamental coupling equations were derived for the general interface node arrangement presented in Fig. 2. Plate nodes A–C are located on the boundary of a plate element that is adjacent to a solid element region. Point i is situated on the intersection between line A–C and a line through solid element node P orthonormal to line A–C. Employing the plate shape functions,

$$
\begin{aligned}
N_A &= -0.25(1+\xi_i\xi_A)(1+\eta_i\eta_A)(1-\xi_i\xi_A-\eta_i\eta_A)\\
N_B &= +0.50(1+\xi_i\xi_B)\left(1-\eta_i^2\right) \qquad (1)\\
N_C &= -0.25(1+\xi_i\xi_C)(1+\eta_i\eta_C)(1-\xi_i\xi_C-\eta_i\eta_C)
\end{aligned}
$$

Received May 5, 1997; revision received April 3, 1998; accepted for publication April 27, 1998.

*Research Scientist, Department of Aerospace Engineering; currently Visiting Research Fellow, Center for Hypersonics, University of Queensland, Brisbane, Queensland 4072, Australia. Member AIAA.

†Aerospace Engineer, Department of Aerospace Engineering.

‡Professor, Department of Mechanical Engineering.

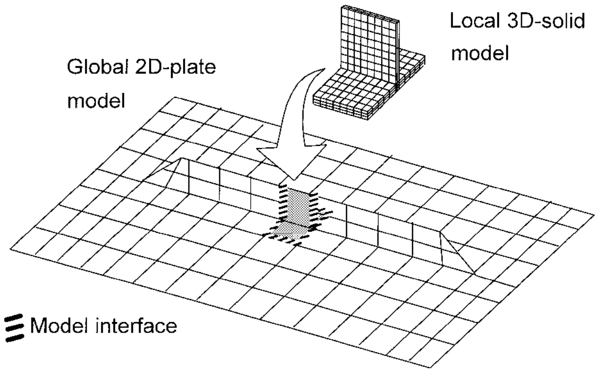

Fig. 1 Global two-dimensional/local three-dimensional analysis methodology.

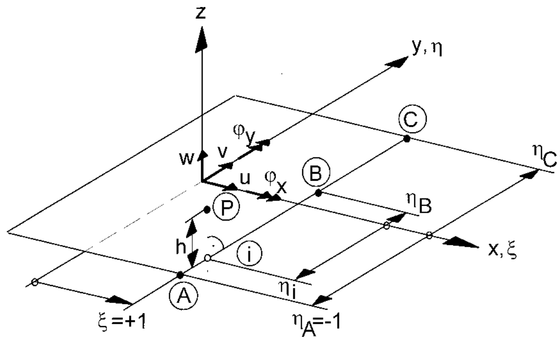

Fig. 2 General interface node arrangement.

the following kinematic relations between nodes A–C and point i can be formulated:

$$
\begin{aligned}
u_i &= N_A \cdot u_A + N_B \cdot u_B + N_C \cdot u_C \\
v_i &= N_A \cdot v_A + N_B \cdot v_B + N_C \cdot v_C \\
w_i &= N_A \cdot w_A + N_B \cdot w_B + N_C \cdot w_C \\
\varphi_{xi} &= N_A \cdot \varphi_{xA} + N_B \cdot \varphi_{xB} + N_C \cdot \varphi_{xC} \\
\varphi_{yi} &= N_A \cdot \varphi_{yA} + N_B \cdot \varphi_{yB} + N_C \cdot \varphi_{yC}
\end{aligned}
\tag{2}
$$

Kinematic relations between solid node P and point i can be formulated by applying the assumptions of Kirchhoff plate theory. Displacements at node P are expressed in terms of displacements and rotations at point i, viz.,

$$
u_P = u_i + h \cdot \varphi_{yi}, \qquad v_P = v_i - h \cdot \varphi_{xi}, \qquad w_P = w_i \tag{3}
$$

Substitution of Eqs. (2) into Eqs. (3) relates degrees of freedom on solid element node P with degrees of freedom on plate element nodes A–C, viz.,

$$
\begin{aligned}
\begin{Bmatrix} u_P \\ v_P \\ w_P \end{Bmatrix} &= N_A \cdot \begin{Bmatrix} u_A \\ v_A \\ w_A \end{Bmatrix} + N_B \cdot \begin{Bmatrix} u_B \\ v_B \\ w_B \end{Bmatrix} + N_C \cdot \begin{Bmatrix} u_C \\ v_C \\ w_C \end{Bmatrix} \\
&+ N_A \cdot h \cdot \begin{Bmatrix} \varphi_{yA} \\ -\varphi_{xA} \\ 0 \end{Bmatrix} + N_B \cdot h \cdot \begin{Bmatrix} \varphi_{yB} \\ -\varphi_{xB} \\ 0 \end{Bmatrix} + N_C \cdot h \cdot \begin{Bmatrix} \varphi_{yC} \\ -\varphi_{xC} \\ 0 \end{Bmatrix}
\end{aligned}
\tag{4}
$$

Thus far the equation development was carried out with reference to a local plate element coordinate system. It is not possible to employ the preceding equations in a general context where element coordinate systems and the global coordinate system often do not coincide. To eliminate this restriction, Eq. (4) was formulated in global coordinates by employing rotation matrix $\boldsymbol{R}^{**}$, viz.,

$$
\begin{aligned}
\begin{Bmatrix} u_P^0 \\ v_P^0 \\ w_P^0 \end{Bmatrix} &= N_A \cdot \begin{Bmatrix} u_A^0 \\ v_A^0 \\ w_A^0 \end{Bmatrix} + N_B \cdot \begin{Bmatrix} u_B^0 \\ v_B^0 \\ w_B^0 \end{Bmatrix} + N_C \cdot \begin{Bmatrix} u_C^0 \\ v_C^0 \\ w_C^0 \end{Bmatrix} \\
&+ N_A \cdot h \cdot \boldsymbol{R}^{**} \cdot \begin{Bmatrix} \varphi_{xA}^0 \\ \varphi_{yA}^0 \\ \varphi_{zA}^0 \end{Bmatrix} + N_B \cdot h \cdot \boldsymbol{R}^{**} \cdot \begin{Bmatrix} \varphi_{xB}^0 \\ \varphi_{yB}^0 \\ \varphi_{zB}^0 \end{Bmatrix} \\
&+ N_C \cdot h \cdot \boldsymbol{R}^{**} \cdot \begin{Bmatrix} \varphi_{xC}^0 \\ \varphi_{yC}^0 \\ \varphi_{zC}^0 \end{Bmatrix}
\end{aligned}
\tag{5}
$$

For a complete discussion of the theory, including the derivation of $\boldsymbol{R}^{**}$, see Ref. 2.

The preceding mathematical approach formed the basis for a generic coupling program that can be used as a preprocessor for a variety of FE codes, viz., MSC/NASTRAN,[3] ABAQUS,[4] etc. The program meets several challenging performance requirements, viz., no limits are imposed on the number of solid elements that can be connected to individual plate elements, generation of coupling equations is automatic with only minimal user input required, and the methodology does not require solver modifications.

With the coupling methodology, the in-plane and out-of-plane displacement fields across two-dimensional/three-dimensional interfaces are maintained in both geometrically linear and nonlinear structural problems.[5] Solid in-plane stress components are computed accurately, directly at the interface. Solid interlaminar stress components converge very quickly to the exact three-dimensional stress solution when moving inward from the interface. In test examples, this was true even when the interfaces were situated in panel regions with complex three-dimensional stress fields.[5] In the current panel analyses, three-dimensional stress results were recovered at least five solid elements inward from the interface to minimize the influence of transition disturbances.

Material Model

Aircraft structures that are made from graphite/epoxy composites are generally designed such that graphite fibers carry most of the applied load. The associated in-plane material behavior is fiber dominated. In a classical composite design, a strain limit of approximately 0.4% is applied to prevent fiber breakage. Within this strain limit, composites behave essentially linear elastically, and their material behavior can be mathematically expressed with nine elastic constants. The current test panels were made from graphite/epoxy T300/914C. Elastic constants for this material combination are presented in Table 1 (Ref. 6).

Composite fibers carry considerably less load in situations where a force flow exists through the laminate thickness, i.e., at free edges, at lap joints, or at skin/stiffener interfaces. The associated interlaminar material behavior is matrix dominated and requires a mathematical representation that accounts for the polymer-based epoxy matrix.[7] Experimental tests on graphite/epoxy laminates revealed that they contain nonlinear matrix-dominated material response including yield, strain rate sensitivity, stress relaxation, and creep.[8] Stress–strain curves were recorded that are quantitatively comparable to those recovered for high-temperature alloys. This is surprising when considering the fundamental differences between the atomic and molecular structures of superalloys and composites. It appears, though, that the different micromechanical processes in these materials result in macroscopically similar material responses. In fact,

Table 1 Elastic material constants for T300/914C identified by Benzeggagh et al.[6]

E_{11}, GPa	E_{22}, GPa	E_{33}, GPa	G_{12}, GPa	G_{13}, GPa	G_{23}, GPa	ν_{12}	ν_{13}	ν_{23}
132	9.5	9.4	5.3	7.0	3.4	0.33	0.34	0.48

a theory originally developed by Ramaswamy et al.[9] for analyzing turbine blades can also be employed to simulate the stress–strain response of matrix-dominated composites.

Their theory consists of three coupled-rate-type tensor equations and several model parameters that need to be identified for individual materials (for a detailed discussion see Ref. 9). The first equation represents the constitutive relation between the inelastic strain rate, the deviatoric stress, the back stress, the drag stress, and the effective value of the overstress, viz.,

$$\dot{\varepsilon}^I_{ij} = D_0 \cdot \exp\left[-\frac{1}{2}\cdot\left(\frac{Z^2}{3\cdot K_2}\right)^n\right]\cdot\frac{(S_{ij}-\Omega_{ij})}{\sqrt{K_2}} \tag{6}$$

The second equation models the development of back stress, where back stress is the level to which an applied stress relaxes during a prolonged strain hold, viz.,

$$\dot{\Omega}_{ij} = \tfrac{2}{3}\cdot f_1\cdot\dot{\varepsilon}^I_{ij} - f_1\cdot(\Omega_{ij}/\Omega_s)\cdot\dot{\varepsilon}^I_e + f_2\cdot\dot{S}_{ij} \tag{7}$$

The third equation models work hardening. This is done by introducing a drag stress that depends on the amount of accumulated inelastic work, viz.,

$$\dot{Z} = m\cdot(Z_1 - Z)\cdot S_{ij}\cdot\dot{\varepsilon}^I_{ij}, \qquad Z_{(0)} = Z_0 \tag{8}$$

Stress–strain curves for superalloys typically saturate at a certain stress level, whereas the matrix-dominated stress–strain curves for T300/914C contain some postyield slope. This was accounted for by adding a postyield slope factor to the stresses computed with the original theory, viz.,

$$\sigma^*_{ij} = \sigma_{ij} + C_P\cdot\varepsilon_{ij} \tag{9}$$

The material model parameters for T300/914C can be identified iteratively with combined experimental and numerical procedures that gradually reduce the error between the simulated material response and the experimentally measured material behavior. Detailed descriptions of such procedures, exceeding the scope of this paper, have been published elsewhere.[2,9] Table 2 lists material model parameters recovered for T300/914C.

The developed mathematical material model formed the basis for an ABAQUS material-user routine. The following assumptions were made to simplify FE model implementation:

1) Only matrix-dominated stress terms σ_{22}, σ_{33}, σ_{12}, σ_{13}, and σ_{23} contribute to viscoplastic material behavior.

2) In a first-order approximation, direct stresses σ_{22} and σ_{33} are assumed to be linear functions of direct strains ε_{22} and ε_{33} (Ref. 10).

3) Nonlinear shear behavior is assumed to be identical in all three material planes. (The authors are aware that this is a strong simplification and address the issue in an ongoing research program.)

Based on the listed assumptions, a constitutive model was developed that contains a linear-elastic/orthotropic representation for the direct stress components and a nonlinear-inelastic/isotropic representation for the indirect stress components.

With ABAQUS, FE equations are solved in the time domain employing incremental-iterative solution schemes. The system stiffness matrix is thereby updated at certain time steps during natural time. Material routines called during these updates return stress and strain levels for all Gauss points in the FE model. The material model for T300/914C was implemented by modifying an existing material subroutine previously developed by Trippit and Jones[11] for high-temperature alloys.

A comparison between the measured and simulated composite material behavior over a range of strain rates is presented in Fig. 3. The maximum deviation between the experimental and computational stress–strain curves over the given strain range is less than 5%. Material strength allowables for T300/914C necessary for the computation of failure indices were taken from Ref. 6 (Table 3).

Table 2 Material model parameters for T300/914C

D_0, 1/s	n	f_1, MPa	f_2	m	Z_0, MPa	Z_1, MPa	Ω_s, MPa	C_P, MPa
5e9	0.237	2.4e4	0	0	2.9e5	2.9e5	65	310

Table 3 Material allowables for T300/914C

Material allowable	Symbol	Value, MPa
Tensile strength in fiber direction	X_T	1328
Compressive strength in fiber direction	X_C	1064
In-plane transverse tensile strength	Y_T	71
In-plane transverse compressive strength	Y_C	221
Interlaminar peel strength	Z_T	98
Interlaminar compression strength	Z_C	242
In-plane shear strength	S_{12}	71
Interlaminar 1–3 shear strength	R_{13}	94
Interlaminar 2–3 shear strength	T_{23}	53

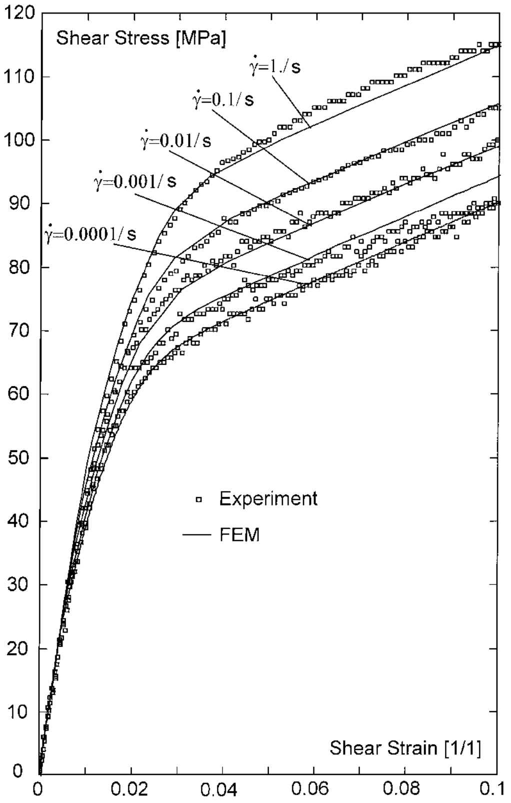

Fig. 3 Measured and simulated shear stress–strain response for T300/914C.

Shear Panel

The first panel analyzed consisted of a quasi-isotropic skin and three blade-type stiffeners that were equally spaced across the working section (Fig. 4). Three panels were fabricated from unidirectional preimpregnated tape. At skin/stiffener interfaces, film adhesive with a woven nylon supporting carrier was used as filling material. To achieve a symmetric stiffener layup, individual skin bays had to be laid up nonsymmetrically with fiber orientations of top plies alternating between +45 and −45 deg. Several skin plies were continued on to the stiffeners to achieve an integral panel layup. The panels were cured in an autoclave with conventional vacuum bagging techniques.

The experimental shear test apparatus consisted of the shear panel, six rosette strain gauges, a picture frame fixture, and two forks, which were held by hydraulic grips. The panel was mounted onto the shear fixture using friction material to prevent slip between the panel and the fixture members. The fixture design allowed the panel corners to pivot but restricted their out-of-plane deformation. This helped to avoid stress concentrations in the specimen corners, which led to premature failure in previous panel tests.

Three panels were tested on a 200-kN servohydraulic uniaxial testing machine. The machine was configured to load in tension employing a constant ramp loading generator in the displacement

Table 4 Summary of shear panel results

Parameter	Experiment A	Experiment B	Experiment C	Experimental average	FE model results	Difference between FE model and experiment, %
Load rate, mm/min	0.3	0.3	0.3			
Temperature, °C	21	25	25			
Rel. humidity, %	50	30	30			
Initial bending, kN	26	25	25	25.33	20	−21
Initial buckling, kN	30	31	30	30.33	30	−1
First crack, kN	63	62	64	63.00	58	−8
Ultimate failure, kN	78	68	79	75.00	N/A	
Comments	Load hold at 10-kN increments	Continuous loading	Load hold at 10-kN increments			

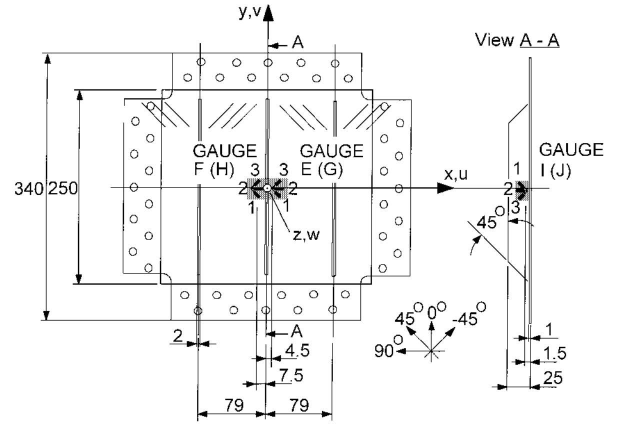

Drawing not to scale
All dimensions in mm
/ / / , \ \ \ = Fibre orientation of top skin plies
▨ Position of local 3D-solid finite element model

Fig. 4 Panel geometry and instrumentation.

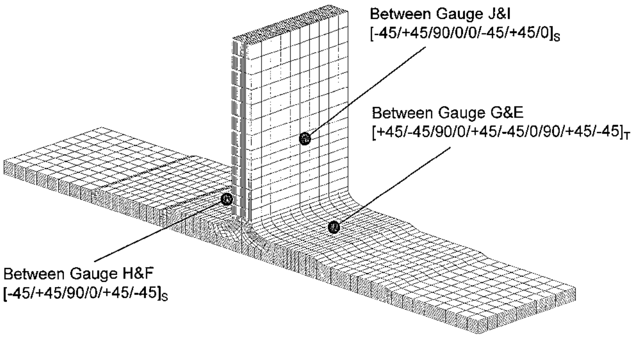

Fig. 5 Local three-dimensional FE model.

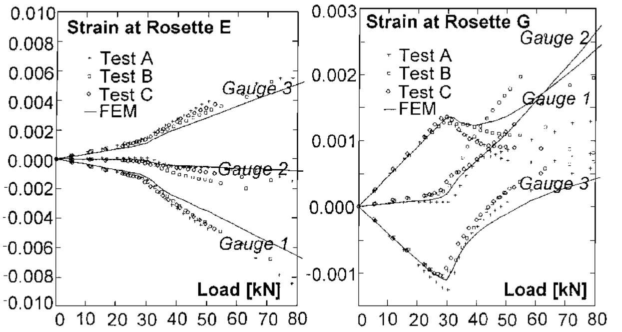

Fig. 6 Experimental and computational strain results at strain gauge rosettes E and G.

control mode. A uniaxial quasistatic load was applied diagonally through the top and bottom pins of the shear fixture until panel failure occurred.

A global two-dimensional plate FE model was developed to represent the shear panel, shear fixture, and load/support conditions imposed by the testing machine. Skin and stiffeners were modeled with plate-type elements. The shear fixture was modeled with beam-type elements. The critical panel region was discretized with a local three-dimensional solid model (Figs. 4 and 5). Individual plies were modeled by single layers of solid elements. Critical areas such as ply dropoffs and the resin-rich area in the Bermuda Triangle at the web/flange transition were modeled according to the cross-sectional details taken from a microscopic photograph. The global two-dimensional plate model and the local three-dimensional solid model were connected with the coupling methodology presented earlier.

Experimental and computational strain results for rosettes E and G are presented in Fig. 6. Strain distribution within panels was relatively homogeneous at prebuckling loads. Strain gauge readings were as such not strongly influenced by small variations in strain gauge placement. Strain distribution within panels was less homogeneous at postbuckling loads. Strong strain gradients occurred, especially around buckles. Consequently, strain gauge readings from this load domain were more sensitive to small variations in strain gauge placement.

At a load level of 60 kN, the maximum deviation between the average experimental strain curves and the computational strain curves was on the order of 20%. At this load level, audible cracks indicated failure initiation. For loads in excess of this value, the experimental strain readings were scattered. Three-dimensional stresses were computed for the critical skin/stiffener domain in the center of the panel. These stresses were substituted into a three-dimensional composite failure model by Tsai et al.,[12] and a failure analysis was carried out. Experimental and computational results are summarized in Table 4.

The computational value for failure initiation compares very favorably with experimental results and contains only 8% error. This is surprising considering that the computational strains contained an error of 20% (Fig. 6). One explanation could be that the employed material allowables did not accurately represent the actual material behavior. This would have led to a partial correction of the computational stress/strain error in the failure analysis.

Elements within the skin/stiffener transition region with failure indices exceeding 1 are plotted as dark areas in Fig. 7. All four ply dropoffs and also some of the curved plies at the web/flange transition appeared to be critical. Critical stress levels occurred in elements representing the +45-deg second from top ply left of the central stiffener and in elements representing the +45-deg top ply right of the central stiffener. Stress results recovered from element centroids indicated that these plies would have undergone compression-type failure.

It is of concern that the continuously loaded panel failed at approximately 15% less applied load than the incrementally loaded panels. However, because no computational postfailure analysis was carried out, it was not possible to determine whether the apparent differences in ultimate load between the tested panels were caused by manufacturing problems or whether this was a consequence of different load histories.

Compression Panel

The second panel analyzed consisted of a quasi-isotropic skin and five blade-type stiffeners equally spaced across the working section.

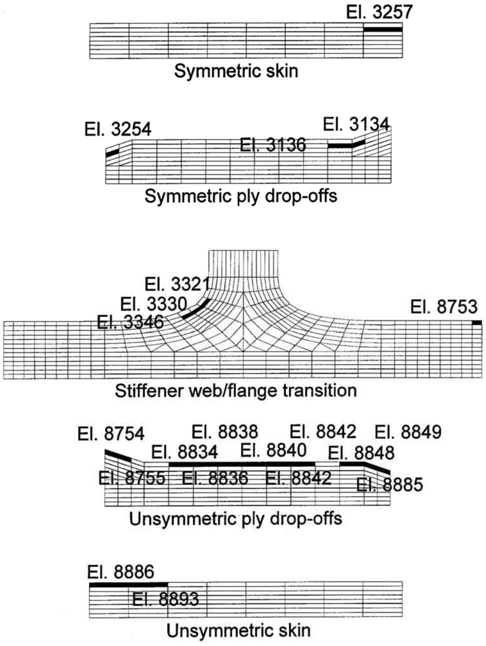

Fig. 7 Computational failure locations in shear panel.

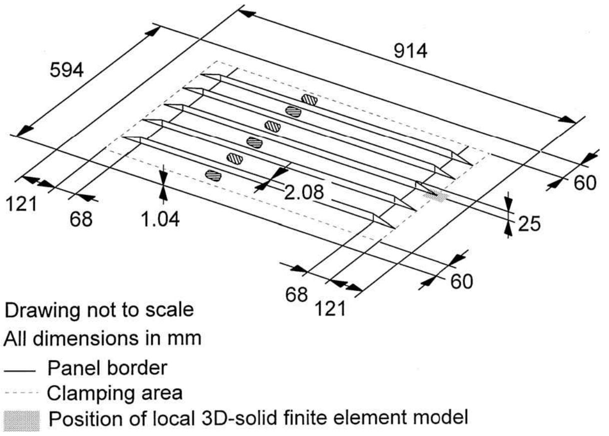

Fig. 8 Compression panel geometry.

Table 5 Experimental failure loads for compression panel

Panel number/failure load, N/mm					Average value, N/mm
BP01	BP03	BP06	BP06B	BP10	
204	184	211	187	158	188.8

Table 6 Computational failure loads for compression panel

Failure theory	Failure load, N/mm	Deviation from experiments, %
Tsai–Wu[12]	151	−20
Maximum Stress[13]	154	−19
Hill[14]	128	−32
Hoffman[15]	178	−5
Hashin[16]	158	−16
Quadratic Stress[17]	158	−16

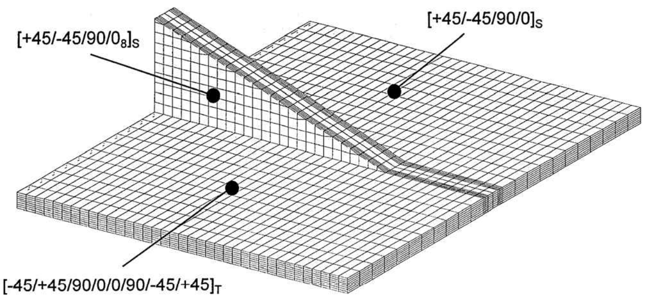

Fig. 9 Local three-dimensional solid FE model.

A total of five panels were manually laid up and cured in an autoclave using hard tools. The panels were made larger than the actual working section to allow their attachment to a box beam test rig. Stiffener ends were trimmed to avoid interference with the test rig. For a description of panel geometry refer to Fig. 8.

Skin bays between the stiffeners were made from eight plies of unidirectional tape. Stiffeners were made from 16 plies. The top three skin plies were laid on top of a 0-deg stringer sublaminate. The requirement of having a symmetric stiffener layup resulted in a skin layup that alternated between being symmetric in some skin bays and unsymmetric in other skin bays.

All panels were structurally tested utilizing a four-point box beam test rig. The test rig consisted of a three-bay aluminum box beam, a supporting steel frame, and two 20,000-lb load jacks, which operated in load control. The middle bay of the box beam contained a detachable skin, which allowed for different test panels to be mounted via a mechanical fastening system. During operation the jacks induced a constant bending moment into the middle bay. Employing this setup, the test panels were loaded by a distributed force that acted in the plane of the panel skin. During tests, failure loads were recorded when first cracks were audible (Table 5).

A global two-dimensional plate FE model was developed that represented the compression panel as well as the loading and support conditions imposed by the box beam test rig. The critical panel region at the central stiffener runout was discretized with a local three-dimensional solid model (Figs. 8 and 9). Individual plies were modeled with separate layers of hexagonal solid elements, with each solid element representing a discrete amount of ply material with constant fiber orientation. Pentagonal solid elements were employed in some regions to generate an overall rectangular solid mesh. The global two-dimensional and local three-dimensional models were connected with the coupling methodology presented earlier.

In a geometrically nonlinear/material linear analysis with NASTRAN, an exponential increase in interlaminar stresses was observed in the vicinity of the stiffener tip, indicating a potential stress singularity at that location. This interpretation was verified by carrying out numerical convergence tests with different stiffener mesh sizes. Here it was found that some interlaminar stress components at the stiffener tip increased dramatically when reducing mesh size. The NASTRAN stress results could, therefore, not be utilized for a failure analysis. The problem was overcome when carrying out a FE analysis with ABAQUS that employed the new viscoplastic material model and the actual panel load history during natural time. In this simulation the material plastified in the critical region and load was shed to less stressed areas. This essentially made the interlaminar stress components nonsingular.

Stress results from the ABAQUS analysis were employed in combination with a selection of failure theories for the computation of failure indices and failure loads. For a comparison between computational and experimental failure loads refer to Table 6 (Refs. 12–17). The computational results for failure initiation compare well with the experimental results. They contain an average error of approximately 22%. However, these results should be considered with caution because of approximations that were made in the development of the FE model, viz., the geometry in the stiffener tip was discretized only approximately, and some severe approximations were made during FE implementation of the nonlinear material model. A certain expected mismatch between the employed material allowables and the actual material behavior further reduces the reliability of computational failure loads.

At design load $N = 200$ N/mm, critical stress levels occurred only within a very small structural domain in the vicinity of the stiffener runout tip. Four critical sections of solid elements within the stiffener

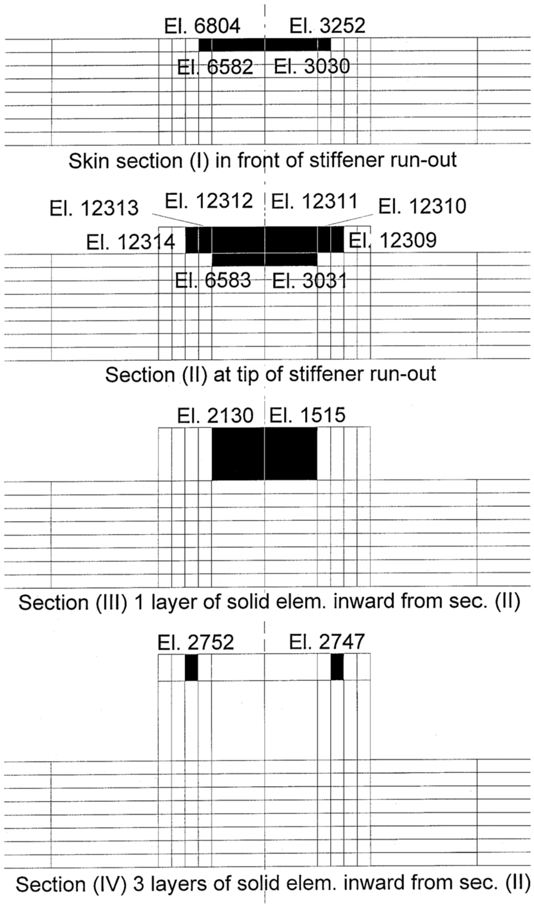

Fig. 10 Computational failure locations in compression panel.

tip region are shown in Fig. 10. The dark areas represent FEs with failure indices exeeding 1. Critical stress levels were found within 0-deg stiffener and 0-deg skin plies and also within 90-deg stiffener plies.

Inspection of stress components within critical elements revealed that three simultaneous failure mechanisms were active at the stiffener runout, viz., 0-deg skin plies under the stiffener failed in a pure in-plane compression mode and combined compression and shear mode, 0-deg stiffener plies failed due to in-plane shear, and 90-deg stiffener plies failed due to interlaminar shear.

These findings led to the following failure interpretation: Panel loading through a skin with relatively small bending stiffness resulted in strong skin-bending deformations at the stiffener runout. This in turn resulted in high-compression stress being induced in the upper 0-deg plies at the stringer/skin transition. Loading through the skin also generated a lap-joint problem at the stiffener runout. Compressive skin load was thereby carried via shear into the stiff 0-deg stringer sublaminate. One part of this load was transferred through in-plane shear within 0-deg skin/stringer transition plies and another part via interlaminar shear within the 90-deg stiffener plies into the assembly of 0-deg stringer plies.

It was found during postfailure inspection of the experimentally tested panels that the stiffener runout separated from the skin. The stiffener runout also split at the interface between the 0-deg stringer sublaminate and the top three stringer/skin cover plies. Both of these failure mechanisms are consistent with the computational failure modes.

Previous empirical design improvements of the stiffener runout[18] were based on a close inspection of experimental results. Premature failure of compression panels was then overcome by reinforcement of the panel skin and by subdivision of the 0-deg stringer sublaminate. The first measure reduced local skin curvature. The second measure increased the effective shear area, which resulted in a less localized load transfer between skin and stringer. The computational results obtained in the present work support both of these design changes.

Conclusions

The computed stress state in critical panel regions was of a complex three-dimensional nature. This justified employment of a global two-dimensional/local three-dimensional modeling approach. The authors are convinced that with a plate-type FE discretization alone it would not have been possible to capture this complex local structural response in the test panels.

An integral stringer attachment concept employed in the shear panel design effectively reduced interlaminar stresses at the critical location. A linear material model was thereby sufficient for computing critical in-plane stresses and failure loads. Employment of a linear material model in the analysis of the compression panel led to interlaminar stress results that were singular. A material nonlinear analysis incorporating the new viscoplastic material model produced stress results that could be employed for a failure analysis of the compression panel.

Computational results for failure location and failure mode appear to be trustworthy because they compare very well with experimental observations. Computational results for failure loads should be treated with caution because of approximations made in the FE models and in the nonlinear material model. Reliability of computational failure loads is also reduced by uncertainties related to the material allowables. The developed methodology should consequently not be employed as a stand-alone tool but in parallel with experimental work.

Acknowledgments

The work presented here was supported by the Cooperative Research Centre for Aerospace Structures (CRC-AS). The CRC-AS is a research initiative between several Australian universities and industry organizations. M. L. Scott and D. Kelly supervised parts of the work, and their contributions are greatly appreciated.

References

[1] Card, M. F., and Starnes, J. H., "Current Research in Composite Structures at NASA's Langley Research Center," *Composite Materials and Structures*, No. A89-5169123-24, Indian Academy of Sciences, Bangalore, India, 1988, pp. 5–26.

[2] Alesi, H., "Postbuckling Analysis of 3D Composite Structures," Ph.D. Dissertation, Dept. of Aerospace Engineering, Royal Melbourne Inst. of Technology, Melbourne, Australia, July 1996.

[3] "MSC/NASTRAN Version 66A User Manual," Vols. 1 and 2, edited by M. A. Reymond, MacNeal–Schwendler Corp., Los Angeles, CA, 1989.

[4] "ABAQUS Version 5.3 User Manual," Vols. 1 and 2, Hibbitt, Karlsson, and Sorensen, Inc., Pawtucket, RI, 1993.

[5] Alesi, H., Jones, R., and Mileshkin, N., "A Technique for Coupling Plate and Solid Elements," *Computational Mechanics*, Vol. 1, edited by S. N. Atluri, G. Yagawa, and T. A. Cruse, Springer–Verlag, New York, 1995, pp. 702–707.

[6] Benzeggagh, M. L., Khellil, K., and Chotard, T., "Experimental Determination of Tsai Failure Tensorial Terms F_{ij} for Unidirectional Composite Materials," *Composites Science and Technology*, Vol. 55, No. 2, 1995, pp. 145–156.

[7] Mills, N. J., *Plastics: Microstructure, Properties and Applications*, Metallurgy and Materials Science Series, edited by R. W. K. Honeycombe and P. Hancock, Edward Arnold, London, 1986, pp. 153–173.

[8] Jones, R., Chiu, W. K., Alesi, H., and Galea, S., "A Preliminary Study into the Matrix Dominated Nonlinear Behavior of Graphite/Epoxy Laminates," *Composite Structures*, Vol. 30, No. 2, 1995, pp. 193–199.

[9] Ramaswamy, V. G., Stouffer, D. C., and Laflen, J. H., "A Constitutive Model for the In-Elastic Multiaxial Response of René 80 at 871C and 982C," *Journal of Engineering and Materials Technology*, Vol. 112, No. 3, 1990, pp. 281–286.

[10] Jones, R. M., *Mechanics of Composite Materials*, International Student ed., McGraw–Hill Kogakusha Ltd., Tokyo, Japan, 1975, pp. 339–342.

[11] Trippit, B. J., and Jones, R., "Recent Australian Developments in the Engineering Applications of Constitutive Modeling," *Numerical Implementation and Application of Constitutive Models in the Finite Element Method*, AMD-Vol. 213/MID-Vol. 63, edited by J. A. Sherwood and M. Sheh, American Society of Mechanical Engineers, New York, 1995, pp. 14–20.

[12] Tsai, S. W., and Wu, E. M., "A General Theory of Strength for Anisotropic Materials," *Journal of Composite Materials*, Vol. 5, Jan. 1971, pp. 58–80.

[13] Zocher, M. A., and Allen, D. H., "Evaluation of First Ply Failure in a Three-Dimensional Loadspace," *Journal of Composite Materials*, Vol. 29, No. 12, 1995, pp. 1649–1665.

[14] Hill, R., *The Mathematical Theory of Plasticity*, Oxford Engineering Science Series, Clarendon, Oxford, England, UK, 1950, p. 317.

[15] Hoffman, O., "The Brittle Strength of Orthotropic Materials," *Journal of Composite Materials*, Vol. 1, April 1967, pp. 200–206.

[16] Hashin, Z., "A Failure Criteria for Unidirectional Fiber Composites," *Journal of Applied Mechanics*, Vol. 47, No. 2, 1980, pp. 329–334.

[17] Brewer, J. C., and Lagace, P. A., "Quadratic Stress Criterion for Initiation of Delamination," *Journal of Composite Materials*, Vol. 22, Dec. 1988, pp. 1141–1155.

[18] Trentin, C., Scott, M. I., and Alesi, H., "Postbuckling Behavior of Blade-Stiffened Fibre Composite Panels," *Proceedings of the 9th International Conference on Composite Materials in Madrid-Spain*, edited by A. Miravete, Woodhead Publishing, Cambridge, England, UK, 1993, pp. 511–518.

G. A. Kardomateas
Associate Editor